





## Nanostructured jumping-droplet thermal rectifier

Ji-Xiang Wang <sup>1,\*</sup> Patrick Birbarah <sup>1</sup> Donald Docimo <sup>1,2</sup> Tianyu Yang,<sup>1</sup>  
Andrew G. Alleyne,<sup>1,†</sup> and Nenad Miljkovic <sup>1,3,4,5,‡</sup>

<sup>1</sup>*Mechanical Science and Engineering, University of Illinois at Urbana Champaign, Urbana, Illinois 61801, USA*

<sup>2</sup>*Department of Mechanical Engineering, Texas Tech University, Lubbock, Texas 79409, USA*

<sup>3</sup>*Electrical and Computer Engineering, University of Illinois at Urbana Champaign, Urbana, Illinois 61801, USA*

<sup>4</sup>*Materials Research Laboratory, University of Illinois at Urbana Champaign, Urbana, Illinois 61801, USA*

<sup>5</sup>*International Institute for Carbon Neutral Energy Research (WPI-I2CNER), Kyushu University, 744 Moto-oka, Nishi-ku, Fukuoka, 819-0395, Japan*



(Received 21 November 2020; revised 3 February 2021; accepted 4 February 2021; published 26 February 2021)

Analogous to an electrical rectifier, a thermal rectifier (TR) can ensure that heat flows in a preferential direction. In this paper, thermal transport nonlinearity is achieved through the development of a phase-change based TR comprising an enclosed vapor chamber having separated nanostructured copper oxide superhydrophobic and superhydrophilic functional surfaces. In the forward direction, heat transfer is facilitated through evaporation on the superhydrophilic surface and self-propelled jumping-droplet condensation on the superhydrophobic surface. In the reverse direction, heat transfer is minimized due to condensate film formation within the superhydrophilic condenser and inability to return the condensed liquid to the superhydrophobic evaporator. We examine the coupled effects of gap size, coolant mass, heat transfer rate, and applied electric field on the thermal performance of the TR. A maximum thermal diodicity, defined as the ratio of forward to reverse heat transfer, of 39 is achieved.

DOI: [10.1103/PhysRevE.103.023110](https://doi.org/10.1103/PhysRevE.103.023110)

### I. INTRODUCTION

The invention of nonlinear solid-state equipment, such as the two-electrode valve known as the electrical rectifier (ER), has enabled the proliferation of modern electronics. Analogous nonlinear devices [1] within the thermal domain which can control the direction of heat flow have enormous potential in modern thermal and heat transfer applications such as electronics thermal management, device reliability, mobile electrification, energy storage, thermal memory, and many more [2,3]. Similar to the ER, a thermal rectifier (TR) enables heat to flow in a specific direction from one terminal to another where the thermal conductivity in the preferential direction is relatively high when compared to the reverse direction. In contrast, the TR prevents heat from flowing in the reverse direction [4]. The thermal diodicity (TD)  $\zeta$  of a TR can be defined by Eq. (1) to reflect the anisotropy in thermal transport:

$$\zeta = (x_{\text{for}} - x_{\text{re}})/x_{\text{re}}, \quad (1)$$

where  $x_{\text{for}}$  is the critical heat transport parameter in the forward direction, and  $x_{\text{re}}$  is the same parameter in the reverse direction. The critical parameter can be the effective thermal

conductivity or heat flux. Past work on TR prototypes has demonstrated effectiveness [Eq. (1)] ranging from 0 to more than 100 [5–7]. There are three major types of TRs based on the principle or operation: (1) solid state, (2) radiation, or (3) phase change.

A solid-state TR typically adopts temperature-dependent heat conduction behavior where transports of photons and electrons are involved to realize an asymmetrical thermal conductivity in opposing directions subjected to a large enough temperature gradient [8,9]. A past study used Fourier's law to theoretically propose an optimization method to boost the effectiveness of a TR made of two terminals whose thermal conductivities have either a linear or a quadratic relationship with temperature [10]. The calculated thermal rectification ratio, similar to the effectiveness [Eq. (1)], can reach 0.5 to 0.86. A follow-up study proposed a TR made from two cobalt oxides, reporting an effectiveness approaching 1.43 at a temperature difference of approximately 60 °C [2]. Using phonon transport, a nanostructured solid-state TR was developed with an effectiveness of 0.02 at room temperature [5]. To increase the effectiveness of solid-state TRs, researchers have explored shape-memory alloy springs to control the movement of two copper blocks [11]. In the forward direction, the two metal blocks touch each other to realize a high thermal conductivity, while the two blocks are separated with an air gap to cause a low effective thermal conductivity in the reverse direction. The experimentally calculated effectiveness was shown to be as high as 93. Others have adopted nanotechnology to experimentally fabricate a microscale–nanoscale metal-insulation superconductor, which consists of a solid-state TR whose effectiveness could reach 140 [12].

\*Present address: College of Electrical, Energy and Power Engineering, Yangzhou University, Yangzhou, 225009, People's Republic of China.

†alleyne@illinois.edu

‡nmiljkov@illinois.edu

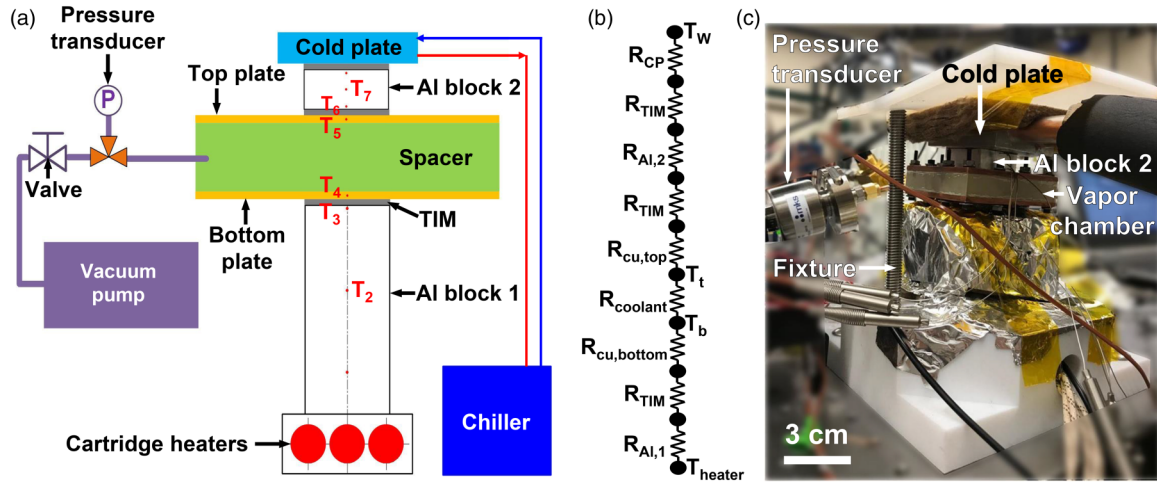


FIG. 1. (a) Schematic of the experimental setup with (b) thermal-node network demonstrating all thermal resistances, and (c) isometric photographic view of the experiment. Schematic in (a) is not to scale. The thermal interface material [TIM, gray color in (a)] was applied to all interfaces between components.

In addition to solid-state TR as developed, showing effectiveness approaching 0.41 [13]. Others have investigated the mechanisms governing nonlinearities in doped silicon films for radiative TR development, focusing on the effects of film thickness and vacuum gap distance [14], achieving an optimized effectiveness of 0.5 at a temperature difference of 100 °C. Generally, past work has shown that photonic-based TRs developed so far have poorer performance when compared to TRs using integrated photon-electron effects [13].

Phase-change TRs represent the third type which exploit the phase-dependent heat transfer capability of phase-change materials to realize nonlinear control of heat flow. Phase transitions from solid to solid [15], solid to liquid [16], and liquid to vapor [17–19] have all been used to develop TRs. The liquid to vapor TRs, which are usually thermosiphons or asymmetric heat-pipes, have been shown to have high thermal rectification. An asymmetric heat-pipe based TR using coalescence-induced droplet jumping, was conceptually designed and theoretically analyzed [20]. Infrared imaging was used to illustrate thermal rectification of the jumping-droplet TR comprising two parts: the condenser where condensation heat transfer leads to a phase transition from vapor to liquid, and the evaporator where liquid to vapor phase change occurs. Functional materials and surfaces have been used to further facilitate or suppress phase-change processes in TRs. A superhydrophobic surface which can attain self-propelled dropwise condensation further enhances energy transport and enables wickless condensate transport to the evaporator, while a superhydrophilic surface facilitates enhanced liquid to vapor phase change via contact line augmentation [20]. Past work on a 1-hexadecanethiol-coated superhydrophobic and a sintered-copper superhydrophilic wick were integrated for a vapor chamber geometry [21], with effects of noncondensable gas, orientation, and wick thickness analyzed.

Recently, nanostructured copper oxide (CuO) functional surfaces have proven to be suitable superhydrophobic and superhydrophilic surfaces due to their ease of manufacturability, cost-effectiveness, and scalability [22]. These CuO-structured surfaces have been shown to enable droplet jumping [23], as

well as droplet electrostatic charging [24]. They have also been used to achieve active hot-spot thermal management of multiple high-power gallium nitride (GaN) transistors, attaining maximum heat fluxes of 13 W/cm<sup>2</sup> [25]. Here, we use CuO nanostructures to develop enclosed vapor chambers composed of superhydrophobic and superhydrophilic surfaces to obtain both enhanced evaporation and condensation heat transfer, as well as thermal rectification. The superiority of adopting CuO as a functional material is presented along with the mechanistic understanding of the effects on thermal transport and rectification of: gap distance between evaporator and condenser, coolant mass, heat transfer rate, and electric field strength. The results presented here provide design guidelines which enable the further optimization of phase-change based jumping-droplet TRs.

## II. EXPERIMENTS

### A. Experimental setup

Figure 1 shows the setup including a schematic of the apparatus [Fig. 1(a)], the system thermal resistance network [Fig. 1(b)], and a photograph of the physical experiment [Fig. 1(c)]. A cartridge heater heat source, composed of three 500-W cartridge heaters (CSS-505500, Omega) inserted into the lower part of a 8.1 cm × 5.0 cm × 9.1 cm aluminum (Al) block (9246K682, McMaster) was used to supply the heat to the vapor chamber, which is composed of a PEEK spacer (8504K36, McMaster), and a top and bottom copper (Cu) plate (9053K22 McMaster). Using Fourier’s law, Al blocks 1 and 2 (9246K15, McMaster) were used to measure the heat flux into and out of the vapor chamber through vertically inserted thermocouples [red dots in Fig. 1(a), TJ36-CAIN-020G-6, Omega]. The temperature of the top and bottom surfaces of the vapor chamber [ $T_t$  and  $T_b$  in Fig. 1(b)] were calculated from measuring  $T_4$  and  $T_5$ , and calculating the heat flux using Fourier’s law. The temperatures  $T_4$  and  $T_5$  were measured using thermocouples (TJ36-CAIN-020G-6, Omega) inserted into the Cu plates (the top and bottom plates), where the distance between the plate surface and the thermocouple,

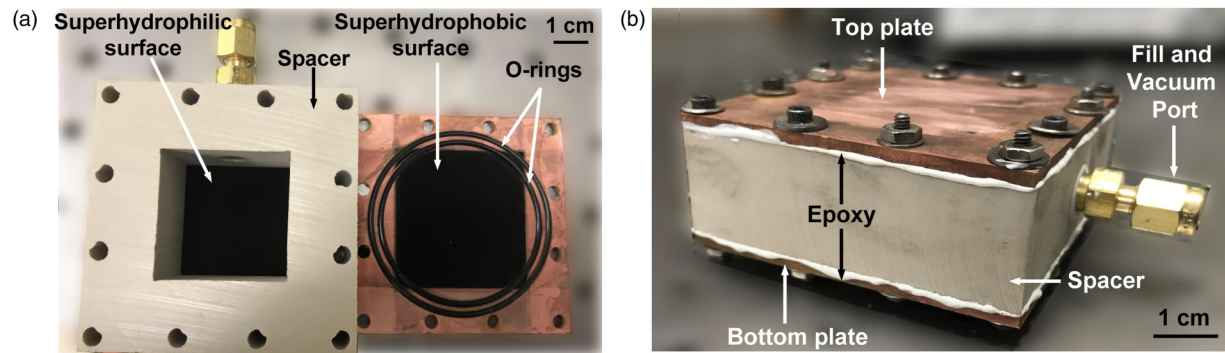


FIG. 2. Photographic view of the vapor chamber (a) prior to assembly showing the spacer (left) and top Cu surface (right), and (b) after assembly and fastening.

$\delta$ , was 0.5 mm. The cold plate (CP20G01, Lytron) was fixed to the top Al block to conduct the generated heat to the chiller (LCK4909-14-0026, Lauda).

To ensure good thermal contact, a thermal interface material (TIM) made from a silicon grease material (Arctic Silver 5) was applied to the interfaces between components. The TIM was applied by dabbing a small amount of TIM material on the surface, and using a credit card to carefully smear the TIM such that thicknesses ranging from 50 to 200  $\mu\text{m}$  were attained. The vacuum pump (model Alcatel 2005, Adixen) was used to depressurize the vapor chamber to an acceptable low pressure ( $\sim 1$  Pa) when the valve is in its “on” state. During the thermal experiments, the valve was in the “off” state to prevent vapor leakage. To ensure vacuum compatibility, the valve was a diaphragm valve (4566K11, McMaster) from which the leak pressure under vacuum was low enough to be ignored for the typical durations of our experiments. A rotary vane pump was selected due to its compatibility with water vapor during pump down and ease of purging after oil-water saturation. A pressure transducer (902B, MKS) is attached to the outlet of the chamber via a T section to obtain the real-time pressure inside of the chamber during degassing and liquid fill. As shown in Fig. 1(b), steel bolts (91251A078, McMaster) and nuts (91240A005, McMaster) were used to fasten the components of the setup tightly to decrease the overall thermal resistance further, and to ensure a leak-tight seal. The real-time data including the detected temperature, pressure, and heater power were collected by a data acquisition system (DAQ, cDAQ-9174, 783729-01, 785185-01, National Instruments).

Figure 2 shows the internal and external structure of the vapor chamber. In order to minimize vapor leakage during experiments, multiple bolts and nuts, with double O-ring seals (9452K123, McMaster) and epoxy (PUDUO, Amazon) were applied to seal the vapor chamber. A Swagelok compression fitting port was used to fill the coolant into the chamber and to pull vacuum in order to degas the system. The internal surfaces [two black surfaces in Fig. 2(a)] were superhydrophilic and superhydrophobic surfaces. The size of the working area of both surfaces was 3.3 cm  $\times$  3.3 cm.

The CuO-based superhydrophilic surface was fabricated according to the following steps: (1) the polished Cu plate (99.9% purity, rms roughness of 10 nm) was ultrasonically cleaned with acetone (CAS 67-64-1, Fisher Scientific) for at

least 5 min and then rinsed with ethanol (CAS 64-17-5, Fisher Scientific), 2-propanol (CAS 67-63-0, Fisher Scientific), and deionized (DI, CAS 7732-18-5, Fisher Scientific) water. (2) The samples were immersed in a hydrochloric acid (CAS 7647-01-0, Fisher Scientific) solution (2 Mol) for 30 s to remove the oxide on the surface, and then rinsed with DI water, and blow dried with a clean nitrogen gas stream. (3) The oxide-free Cu plates were immersed in a  $96 \pm 3^\circ\text{C}$  alkaline solution for 10 min. The solution was composed of DI water,  $\text{Na}_3\text{PO}_4 \cdot 12\text{H}_2\text{O}$  (Lot No. TBH5019, Sigma), NaOH (Lot No. MKCF1798, Sigma), and  $\text{NaClO}_2$  (Lot No. BCBS2692) (100:10:5:3.75 wt. %). (4) The sample was removed from the alkane solution and immediately rinsed with DI water and dried with a clean nitrogen gas stream. The nanostructured CuO film formed conformally on the Cu surface via a chemical reaction to attain superhydrophilicity, as measured by apparent advancing and receding angles approaching zero.

To render the CuO surface superhydrophobic, the superhydrophilic CuO surface obtained via the previous fabrication steps was functionalized by conformal deposition of heptadecafluoro-1,1,2,2-tetrahydrodecyl trimethoxy silane (HTMS, CAS 83048-65-1, TCI America). Briefly, the superhydrophilic CuO tab was placed in a glass beaker along with a smaller open secondary beaker containing 1 mL of HTMS and toluene (CAS 67-64-1, Fisher Scientific) mixture (5% v/v). A lid fabricated from aluminum foil was placed on top of the large beaker containing the tab and HTMS solution and the beaker then placed in an atmospheric pressure oven (Lindberg Blue M, Thermo Scientific) at  $90 \pm 5^\circ\text{C}$  for 3 h. To characterize the wetting of the superhydrophobic surface, the apparent advancing and receding contact angles with water droplets were measured on a microgoniometer (MCA-3, Kyowa), showing  $170^\circ \pm 5^\circ$  and  $165^\circ \pm 9^\circ$ , respectively.

In order to study the effect of electric field on vapor chamber performance, the Cu top and bottom plates [Fig. 1(a)] were connected to a power source (6033A, Agilent) with a thin layer of Polyimide tape used to insulate the Cu plates from the Al block and to ensure safety.

Scanning electron micrographs (SEMs) of the utilized superhydrophilic and superhydrophobic surfaces are shown in Fig. 3. Multiple magnifications of the superhydrophilic surface are shown in Figs. 3(a) and 3(b), where the nanoblade structures can be observed. Figures 3(c) and 3(d) present SEM images of the superhydrophobic surface after focused

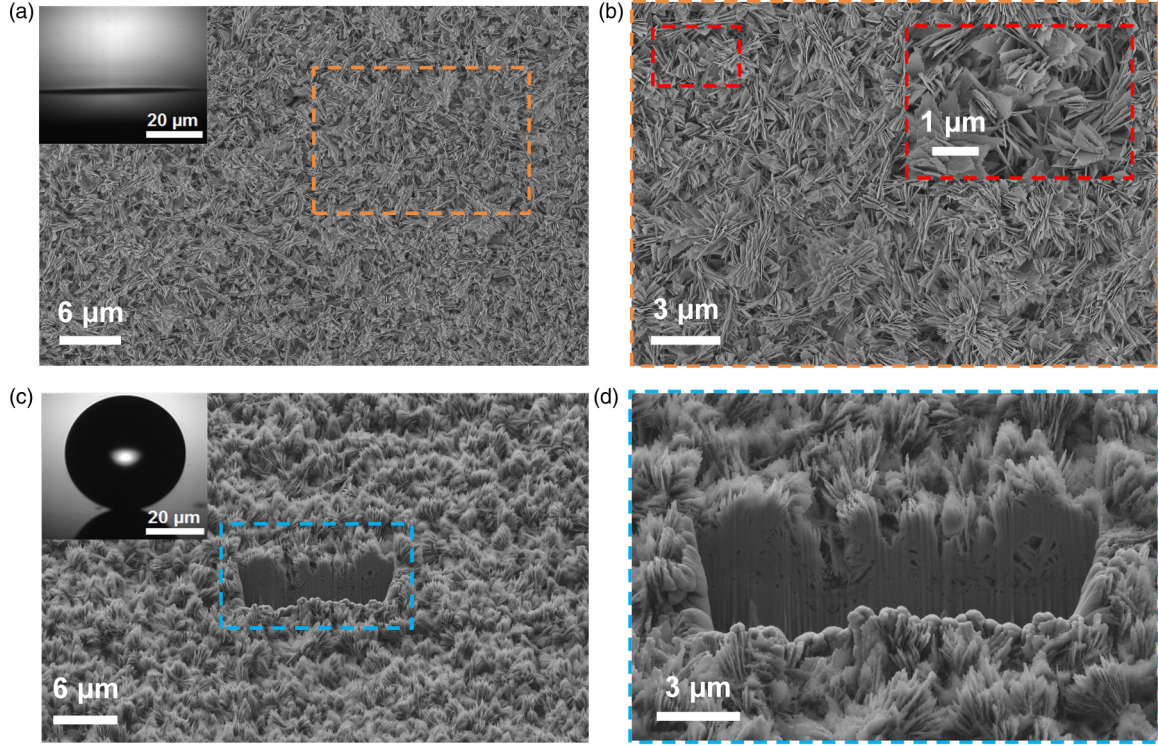


FIG. 3. Top-view SEM images of the adopted nanostructured surfaces. (a) Top-view SEM image of the CuO superhydrophilic surface and contact angle results; (b) dotted orange region in (a) and regions with multiple magnifications; (c) top-view SEM image of the CuO-based superhydrophobic surface with a focused ion-beam milling and contact angle results; (d) dotted blue region in (c).

ion-beam milling (Nvision 40 Dual Beam) to provide a trench of the nanostructured surface and demonstrate the 3- $\mu\text{m}$ -deep CuO-based nanostructures. The milling process was operated with normal incidence of the ion beam with a sample tilt of  $52^\circ$ , ion current of 300 pA, and ion-beam energy of 30 keV.

### B. Data analysis and uncertainty propagation

The critical parameters measured during the experiments to quantify performance are the heat flux ( $q''$ ), average vapor chamber temperature ( $T_{\text{avg}}$ ), effective thermal conductivity ( $k_{\text{eff}}$ ) of the vapor chamber, and overall thermal resistance ( $R_{\text{th}}$ ). The heat flux was obtained from analysis of the inserted thermocouples using Fourier's law. The average temperature of the vapor chamber was calculated using Eq. (2) where  $T_{\text{bot}}$  and  $T_{\text{top}}$  were obtained via Eqs. (2a) and (2b):

$$T_{\text{avg}} = (T_{\text{bot}} + T_{\text{top}})/2, \quad (2)$$

$$T_{\text{bot}} = T_4 - \frac{q''_{2-3}\delta}{k_{\text{cu}}}, \quad (2a)$$

$$T_{\text{top}} = T_5 + \frac{q''_{6-7}\delta}{k_{\text{cu}}}, \quad (2b)$$

where  $\delta$  is the distance between thermocouples 4 and the bottom surface of the chamber [Fig. 1(a)],  $k_{\text{cu}}$  is the intrinsic thermal conductivity of Cu,  $q''_{2-3}$  is the inlet heat flux calculated by  $T_2$  and  $T_3$  [in Fig. 1(a)] using Fourier's law, and  $q''_{6-7}$  is the outlet heat flux calculated by  $T_6$  and  $T_7$ .

The effective thermal conductivity and thermal resistance were calculated using Eqs. (3) and (4):

$$k_{\text{eff}} = \overline{q''}H/|T_{\text{bot}} - T_{\text{top}}|, \quad (3)$$

$$R_{\text{th}} = |T_{\text{bot}} - T_{\text{top}}|/\overline{q''}A, \quad (4)$$

where  $H$  is the height of the vapor chamber [Fig. 1(a)],  $A$  is the overall effective surface area for heat transfer ( $3.3 \text{ cm} \times 3.3 \text{ cm}$ ), and  $\overline{q''}$  is the average of  $q''_{2-3}$  and  $q''_{6-7}$ .

The maximum uncertainty of the individual thermocouple temperature measurements and their spatial location were  $\pm 0.27^\circ\text{C}$  and  $\pm 0.02 \text{ mm}$ , respectively. Prior to experimentation, the thermocouples were calibrated using a high accuracy and high stability bath equipped with a class AA resistance temperature detector having an uncertainty of  $\pm 0.1 + 0.0017T$ , where  $T$  represents the measured value. Thermal conductivity of the Cu was obtained from thermophysical measurements and was  $398 \pm 4 \text{ W}/(\text{m} \cdot \text{K})$ . Equation (5) was used to propagate uncertainties ( $\sigma$ ) for calculated parameters from measured values ( $f$ ) such as heat flux, surface temperature, effective thermal conductivity, and thermal resistance, which has maxima of  $\pm 2.3$ ,  $\pm 4.7$ ,  $\pm 3.2$ , and  $\pm 3.2\%$ , respectively.

$$\sigma_f = \pm \sqrt{\sum_{i=1}^n \left( \frac{\partial f}{\partial x_N} \right)^2 \sigma_{x_N}^2}, \quad (5)$$

where  $\sigma_f$  is the uncertainty of the focused parameter,  $f$  is the focused parameter,  $x_N$  is the  $N$ th variable of the parameter, and  $\sigma_{x_N}$  is the uncertainty of the  $N$ th variable of the parameter.

**C. Experimental methods**

Prior to conducting experiments, preparation of the vapor chamber, including liquid filling and removal of all noncondensable gases, was completed. Removal of all noncondensables was key to obtaining high-fidelity heat transfer measurements due to the elimination of dominant diffusional thermal resistances in the vapor phase [23]. The main procedure used to prepare the vapor chamber is described as follows: (1) the chamber was assembled using the steel bolts and nuts. (2) Prior to tightening of the bolts and nuts, a thin layer ( $\sim 150 \mu\text{m}$ ) of epoxy was carefully applied to the interface between the surface and the spacer edges. (3) The assembled chamber was weighed on an analytical balance (model EX224, OHAUS) after allowing the epoxy to cure for 24 h in the ambient laboratory environment. (4) The valve [Fig. 1(a)] was opened, and the chamber was filled with a metered amount of DI water, followed by valve closing. (5) The chamber was disconnected from the fill line at the valve and weighed again to obtain the added mass of water to a greater degree of precision. (6) The chamber was placed in a freezer (KTUF88, Koolatron) set to a temperature of  $-25 \pm 5 \text{ }^\circ\text{C}$  for at least 40 min to ensure the complete freezing of the filled water. (7) The chamber was removed from the freezer and immediately reconnected to the vacuum pump, the valve was opened, and the vacuum pump turned on. (8) Once the pressure inside the vapor chamber approached 0.1 Pa and was steady at this value for 1 min, the valve was closed. (9) The chamber was allowed to reach room temperature ( $\sim 2 \text{ h}$ ), and steps (6), (7), and (8) were repeated again. (10) After repeating the cycle for a total of five times, the chamber mass was measured one final time to determine the final liquid amount.

After chamber preparation was complete, the chamber was immediately placed and fixed on the thermal test setup [Fig. 1(a)]. The thermal test procedure was conducted as follows: (1) Initialize the DAQ for data collection and storage. (2) Power on the chiller. (3) Regulate the input voltage of the cartridge heaters to 5 V at the beginning and wait until the temperature reaches a stable condition for at least 5 min. (4) Increase the input voltage with small increments (approximately 2 V for each time step) and wait until temperature stabilization is achieved. (5) Repeat step (4) until  $T_4$  exceeds  $100 \text{ }^\circ\text{C}$ . (6) Turn the cartridge heater power off and wait until the experimental system returns to the room temperature ( $\sim 2 \text{ h}$ ). (7) Prepare for the next experimental run to test data repeatability. Before each experiment, steps (6)–(10) were conducted to pump down the chamber if the inside coolant mass remained within 0.5% of the previous experiment. If the coolant mass inside the chamber deviated by more than 0.5%, the next experimental run necessitated that we follow the full set of steps from (1) to (10).

Two operational modes were investigated. The forward mode where the superhydrophilic surface was attached to Al block 1 [bottom block in Fig. 1(a)] and the superhydrophobic surface attached to Al block 2 [top block in Fig. 1(a)]. The

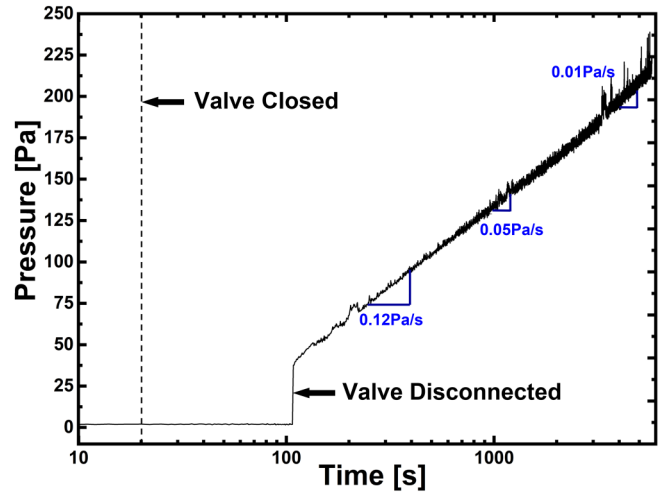


FIG. 4. Pressure leak test showing the transient pressure for the assembled vapor chamber.

reverse mode was also studied where the vapor chamber orientation was reversed.

**III. RESULTS AND DISCUSSION**

Prior to thermal testing, we conducted a leak test of the vapor chamber whose chamber height is 1.9 cm in order to understand the steady leak rate and to gain an awareness of allowable timescale for experiments prior to noncondensable gases biasing our results. Figure 4 shows the measured chamber pressure as a function of time during the leak test, demonstrating a diminishing leak rate (from 0.12 Pa/s at time of 200 s to 0.01 Pa/s at time of 4000 s). Considering the chamber internal volume ( $2.07 \times 10^{-5} \text{ m}^3$ ), the range of volume-integrated leak rate was  $2.07 \times 10^{-7}$  to  $2.48 \times 10^{-6} \text{ Pa m}^3 \text{ s}^{-1}$ . The acceptable volume-integrated leak rate for spacecraft cabin seal valves ranges from  $5.0 \times 10^{-11}$  to  $1.0 \times 10^{-4} \text{ Pa m}^3 \text{ s}^{-1}$  [26], which is acceptable for experiments lasting less than 1 h prior to requiring pump down again to remove noncondensable gases. Based on our previous measurement on steam condensation at saturation pressures approaching the experimentally tested pressures here, experimental values maintain high fidelity as long as the partial pressure of noncondensable gases remains below approximately 8 Pa [27,28]. Given the leak rate at saturation pressure ( $> 1 \text{ k Pa}$ ) approaches  $< 0.001 \text{ Pa/s}$  (Fig. 4), we estimate that the time required to reach the critical noncondensable gas partial pressure where data are not trustworthy to be approximately 2 h, which is less than the experimental test time to reach steady state and acquire data. The jump in pressure once the valve was disconnected occurred because prior to disconnection, both sides of the valve connection were vacuum pressure (one side pump and the other vapor chamber). Once disconnected, the pump side changed to atmospheric pressure, which increased the leak rate. It is important to note that the leak test was conducted with an evacuated chamber, which presents a conservative estimate. During testing, the chamber is filled with saturated vapor at a few kPa vapor pressure, which decreases the leak rate due to the lower pressure difference.

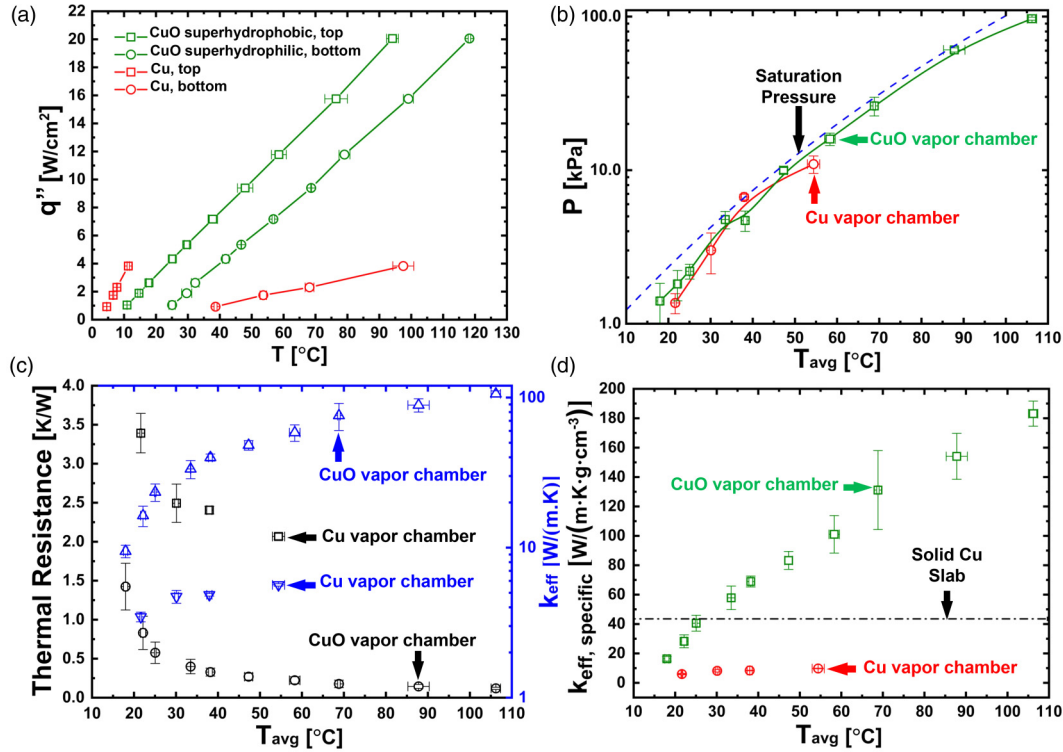


FIG. 5. Thermal performance of the two chambers having either smooth Cu surfaces (labeled as Cu vapor chamber) or superhydrophilic-superhydrophobic surfaces (labeled as CuO vapor chamber) with a gap size of 1.27 cm and a coolant mass of 8 g for each chamber. (a) Heat flux as a function of bottom and top temperature. (b) Chamber pressure as a function of average chamber temperature as calculated by Eq. (2) [Fig. 1(a)]. (c) Thermal resistance and effective thermal conductivity as a function of chamber average temperature. (d) Specific effective thermal conductivity as a function of average chamber temperature.

### A. Mode performance

The thermal testing emphasized the effect of the functional surfaces, coolant mass, gap size, and electric field on the thermal performance of the two modes: forward mode and reverse mode. In order to highlight the advantage of the CuO nanostructured vapor chamber, a chamber with unaltered smooth Cu plates was tested for comparison. Experimental results demonstrating the thermal performance of both chambers is presented in Fig. 5. Figure 5(a) shows the measured heat flux as a function of temperature difference between the top and bottom surfaces for both chambers. The temperature of the bottom surface of the Cu chamber was always higher than that of the bottom CuO nanostructured superhydrophilic surface of the CuO chamber under equivalent heat flux conditions. In contrast, the temperature of the top surface of the Cu chamber was always lower than that of the top CuO superhydrophobic surface of the CuO chamber. The results indicate that for the bottom evaporation and top condensation orientation, heat in the CuO chamber can be transported more efficiently due to the superhydrophilicity facilitating rapid evaporation and the superhydrophobicity promoting efficient condensation. The greater evaporation rate can be understood from the larger wetted area on the superhydrophilic surface, enabling efficient evaporation near the extended three-phase contact line [29–32], while the efficient condensation occurs due to dropwise condensation overcoming the limitations of filmwise condensation [33–39]. Figure 5(b) presents the relationship

between the average temperature [obtained by Eq. (2)] and pressure in the vapor chamber, showing that the pressure curves of the two fabricated chambers coincide with each other. Furthermore, the saturation pressure curve of DI water, calculated according to the average vapor chamber temperature, fit well with the pressure curves of both chambers. The good fit indicated that the working fluid was at saturation conditions and that the average vapor chamber temperature could be used to predict the chamber saturation pressure reasonably well. Figure 5(c) presents the overall thermal resistance and effective thermal conductivity of the two chambers, showing that the thermal performance of the CuO chamber was better than the Cu chamber. The effective thermal conductivity was observed to increase with increasing average temperature for both chambers due to the elevated saturation pressure and hence higher evaporation and condensation rates.

Figure 5(d) shows the specific effective thermal conductivity, defined as the effective thermal conductivity normalized by the overall chamber mass, which is a quantity of importance for mobile systems where high gravimetric power density is required. The specific effective thermal conductivity of the vapor chamber ( $k_{eff, specific}$ ) was compared to the solid Cu intrinsic specific thermal conductivity ( $k_{Cu, specific}$ ) as calculated by Eqs. (6) and (7), respectively:

$$k_{eff, specific} = k_{eff} / \rho_c, \quad (6)$$

$$k_{Cu, specific} = k_{Cu} / \rho_{Cu}, \quad (7)$$

where  $\rho_c$  is the effective density of the vapor chamber defined by the material distribution averaged density ( $\rho_c = m_c/V_{\text{chamber}}$  where  $m_c$  is the mass of the coolant and  $V_{\text{chamber}}$  is the volume of the internal area of the chamber), and  $k_{\text{Cu}}$  and  $\rho_{\text{Cu}}$  are the intrinsic thermal conductivity and density of solid Cu, respectively. The relationship between the specific effective thermal conductivity and average temperature is shown in Fig. 5(d). The CuO vapor chamber has a specific effective thermal conductivity higher than that of solid Cu when the average temperature is higher than 25 °C. The difference between the CuO vapor chamber and intrinsic Cu specific effective thermal conductivity increases as the average temperature rises. The largest measured specific effective thermal conductivity of the CuO vapor chamber was  $183 \pm 8 \text{ W}/(\text{m K g cm}^{-3})$ , a  $3\times$  increase when compared to intrinsic Cu which is  $44 \text{ W}/(\text{m K g cm}^{-3})$ . The specific effective thermal conductivity of the Cu chamber was  $9.86 \text{ W}/(\text{m K g cm}^{-3})$ , lower than the reference line, indicating the thermal performance of the smooth Cu chamber was worse than a solid Cu block.

**1. Effect of coolant mass**

Figure 6 demonstrates the effect of the coolant mass on the thermal performance of the CuO nanostructured chamber with a gap of  $H = 1.27 \text{ cm}$ . Heat flux as a function of the average temperature for various coolant masses is plotted in Fig. 6(a). The heat flux of the four coolant masses was invariant at low average chamber temperatures ( $T_{\text{avg}} \leq 20 \text{ }^\circ\text{C}$ ). The difference in heat flux among the four masses increases when the average temperature rises further. A 4-g coolant mass can acquire a higher heat flux under a comparable average temperature [40]. In contrast, a 12-g coolant mass, which is the highest tested, performed the worst.

Figures 6(b) and 6(c) show the two performance parameters,  $R_{\text{th}}$  and  $k_{\text{eff}}$ , as a function of average chamber temperature, respectively. The thermal resistance tends to be invariant with coolant mass at elevated temperatures ( $T_{\text{avg}} > 30 \text{ }^\circ\text{C}$ ). Similar to the results presented in Fig. 6(c), the thermal resistance reduces as the temperature increases. The maximum thermal resistance was  $1.7 \pm 0.9 \text{ K/W}$  for an average temperature of  $15 \pm 0.2 \text{ }^\circ\text{C}$  and 4 g of coolant mass. When the average temperature exceeded 70 °C, the thermal resistances for the chamber prototypes having various coolant mass all reached a stable low limit of approximately 0.1 ~ 0.2 K/W. Correspondingly, the effective thermal conductivity  $k_{\text{eff}}$  increased with average temperature. Vapor chambers made with a coolant mass of 2 g attained a relatively high  $k_{\text{eff}}$ , indicating that smaller fill ratios (2 g represents 14.5% fill ratio, while 12 g is 87% fill ratio) enhance thermal performance due to the large latent heat of the DI water. The maximum measured effective thermal conductivity was  $100 \pm 11.2 \text{ W}/(\text{m K})$  for a fill ratio at 14.5% at  $T_{\text{avg}} = 88 \pm 3.1 \text{ }^\circ\text{C}$ .

**2. Effect of fill ratio**

The fill ratio of the DI water in the vapor chamber can affect the thermal performance. The variance in the gap size ( $H$ ) differentiates the maximum filling mass. Therefore, the effect of fill ratio, or the ratio of DI water to the total free volume inside the chamber, was investigated. Figures 7(a)–7(c) show

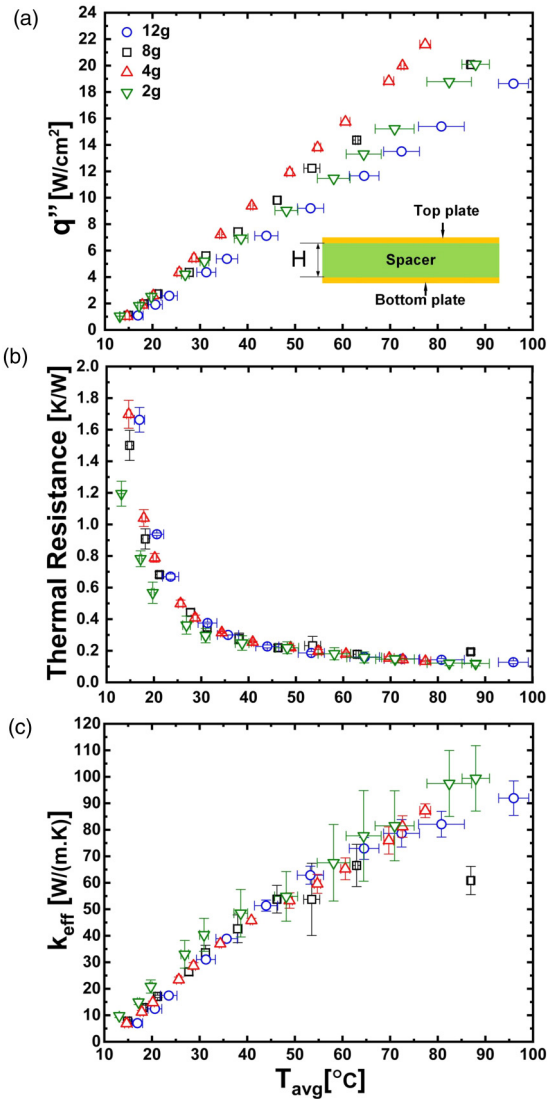


FIG. 6. Thermal performance of the CuO nanostructured vapor chamber for various coolant masses at a gap spacing of  $H = 1.27 \text{ cm}$  (inset schematic). Measured (a) heat flux, (b) thermal resistance, and (c) effective thermal conductivity as a function of average chamber temperature. Inset in (a): Schematic representation of the chamber cross section with a superhydrophobic top plate, and superhydrophilic bottom plate. Gravity points downward in the schematic. Schematic not to scale.

the thermal performance of chambers having two different gap sizes ( $H = 1.27$  and  $2.54 \text{ cm}$ ) with 2 g of coolant, while Figs. 7(d)–7(f) show the results of three different gap sizes ( $H = 1.27, 1.90,$  and  $2.54 \text{ cm}$ ) with 8 g of coolant.

Figure 7 shows that for equivalent coolant mass, a smaller filling ratio contributes to a higher effective thermal conductivity. For instance, a 7.2% fill ratio (2 g coolant with  $H = 2.54 \text{ cm}$ ) has  $k_{\text{eff}} = 138 \pm 1.23 \text{ W}/(\text{m K})$  while a 14.5% fill ratio (2 g coolant with  $H = 1.27 \text{ cm}$ ) has  $k_{\text{eff}} = 86.2 \pm 4.25 \text{ W}/(\text{m K})$ . The results suggest a 50% decrease in the fill ratio can achieve up to a 60% increase in effective thermal conductivity under comparable operating conditions. The potential increase in performance is even higher at larger coolant

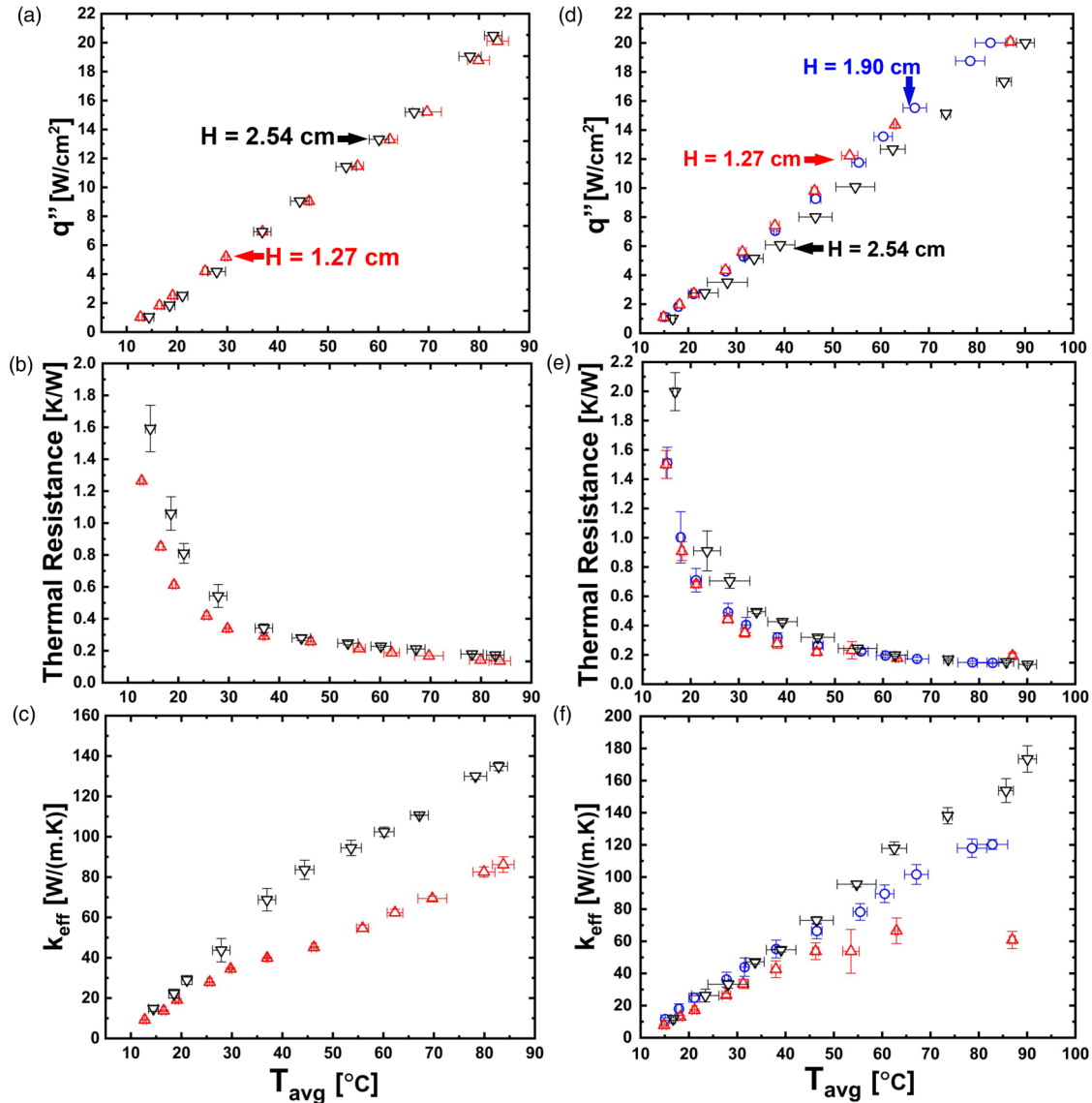


FIG. 7. Thermal performance of vapor chamber prototypes having (a)–(c)  $H = 1.27$  and  $2.54$  cm, with  $2$  g of coolant (DI water), and (d)–(f)  $H = 1.27$ ,  $1.90$ , and  $2.54$  cm with  $8$  g of coolant. The experimental measurements report (a), (d) heat flux, (b), (e) thermal resistance, and (c), (f) effective thermal conductivity, as a function of average chamber temperature.

masses [Figs. 7(d)–7(f)], where up to a 158% enhancement in  $k_{eff}$  can be achieved when the fill ratio is halved.

In general, the effective thermal conductivity is sensitive to the fill ratio of the vapor chamber due to the fact that at high fill ratios, a thick liquid layer above the evaporator surface exists, altering the morphology of the thin liquid film and flooding the evaporator [41].

### 3. Effect of electric field

Jumping droplets generated by dropwise condensation on CuO nanostructured superhydrophobic surfaces are positively charged due to the electrostatic charging [24]. The charge on the droplets enables the external control of these droplets with electric fields. The effect of external electric fields was investigated using the  $H = 1.27$  cm chamber prototype having a 29% fill ratio (Fig. 8). Figure 8(a) shows the transient temperature response when the applied heat flux was  $4.4$  W/cm<sup>2</sup>

while Fig. 8(b) shows the heat transfer results when the heat flux was  $8.8$  W/cm<sup>2</sup>. The measurement thermocouples  $T_5$  and  $T_4$  [Fig. 1(a)] experienced a sudden decrease when the electric field was applied because the inserted thermocouples were affected by the applied electrical potential. Note that thermocouples  $T_5$  and  $T_4$  returned to their normal operating mode when the electrical field was turned off. Temperatures detected by normal-functioning thermocouples had no significant change prior to and after field application, suggesting that the application of the electric field during testing limited the thermal performance characterization of our prototype devices. Based on the low fidelity offered by the thermocouple measurements near the surface, we could not obtain any meaningful implications from the electric field tests, necessitating further future work to integrate electrically insulating thermocouples that have good thermal conductance to the Cu blocks in use.



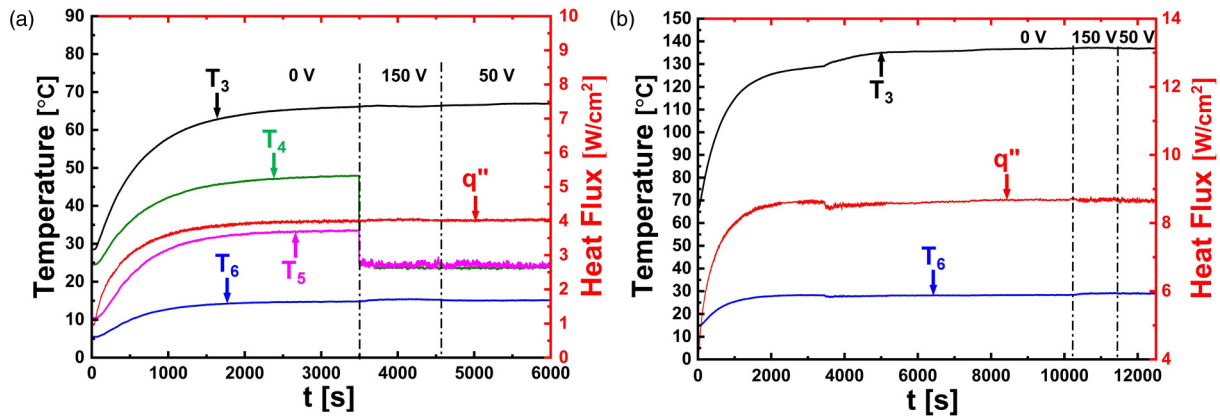


FIG. 8. Transient temperature response with and without electric field for a chamber prototype having  $H = 1.27$  cm with 4 g coolant, at (a) heat flux of  $4 \text{ W/cm}^2$ , and (b) heat flux of  $8.8 \text{ W/cm}^2$ .

**B. Thermal rectification**

Thermal performance in the forward mode was obtained with the chamber top surface consisting of a superhydrophobic CuO surface and the bottom being the superhydrophilic CuO surface. When the top and bottom surfaces are reversed, the vapor chamber exhibits the reverse mode. Comparative studies between these two modes were conducted to analyze the thermal rectification using the thermal-conductivity based TD calculated by Eq. (1).

The effective thermal conductivities of the various vapor chambers as a function of temperature difference are displayed in Fig. 9. For the reverse mode, the effective thermal conductivity remained unchanged for the temperature difference range between 25 and 75 °C, while the effective thermal conductivity for the forward mode increased rapidly for the same range. For a chamber having a fixed mass of coolant, the effective thermal conductivity of a taller chamber (higher  $H$ ) in forward mode is generally larger than that of a shorter chamber (lower  $H$ ) for comparable temperature difference. Figure 9(f) shows that the effective thermal conductivity of the  $H = 2.54$  cm chamber with 8-g coolant mass can achieve  $k_{\text{eff}} = 181 \text{ W/(m} \cdot \text{K)}$ , while in the Fig. 9(e) for  $H = 1.27$  cm with the equivalent mass had  $k_{\text{eff}} = 61 \text{ W/(m} \cdot \text{K)}$  where a 100% increase in the gap size ( $H$ ) can attain a 215% enhancement in effective thermal conductivity. However, for a given  $H$ , increasing the coolant mass enhances effective thermal conductivity. Table I summarizes the thermal-conductivity

based TDs for different test and vapor chamber conditions, where the thermal effectiveness is defined by Eq. (1) using the effective thermal conductivity as the critical transport property. The results indicate that taller chambers consistently obtain higher TDs. When the coolant mass was 8 g, the TD of a shorter chamber (1.27 cm) was 13.8 while the TD of a taller chamber (2.54 cm) is 39. Furthermore, relatively low fill ratios ( $\leq 29\%$ ) have higher TDs ( $\geq 27$ ) while when the fill ratio reaches 58%, the TD decreases to 13.8.

Generally, a taller chamber has a higher thermal-conductivity based TD. This higher TD can be understood from analysis of the effective thermal conductivity and its increase from enlarging the height of the chamber [Eq. (3)]. Therefore, the thermal-conductivity based TD definition can become problematic as a sole benchmark of performance. Figure 10 demonstrates the thermal resistances of the various vapor chamber designs as a function of temperature difference. Similar to Fig. 9, the thermal resistance remains nearly unchanged for the temperature difference range between 25 and 75 °C in the reverse mode. In contrast, the forward mode thermal resistance decreases for the same temperature range. For a fixed mass of coolant, the thermal resistance does not change appreciably by doubling the chamber height ( $H$ ) in the forward mode, which can eliminate the effect of chamber height. For the reverse mode, the thermal resistance of a taller chamber is slightly higher. Figure 10(a) shows that the thermal resistance ( $R_{\text{th}}$ ) of the  $H = 1.27$ -cm chamber with a

TABLE I. Effectiveness of various TRs for temperature differences ranging from 30 to 45 °C.

Gap, $H$ (cm)	Coolant mass (g)	Fill ratio (%)	Thermal-conductivity based TR effectiveness	Thermal-resistance based TR effectiveness
1.27	2	14.5	29.8	27.5
2.54	2	7.23	31.4	31.9
1.27	4	28.9	26.6	24.6
2.54	4	14.5	36.2	36.3
1.27	8	57.8	13.8	23.7
2.54	8	28.9	39.0	36.6

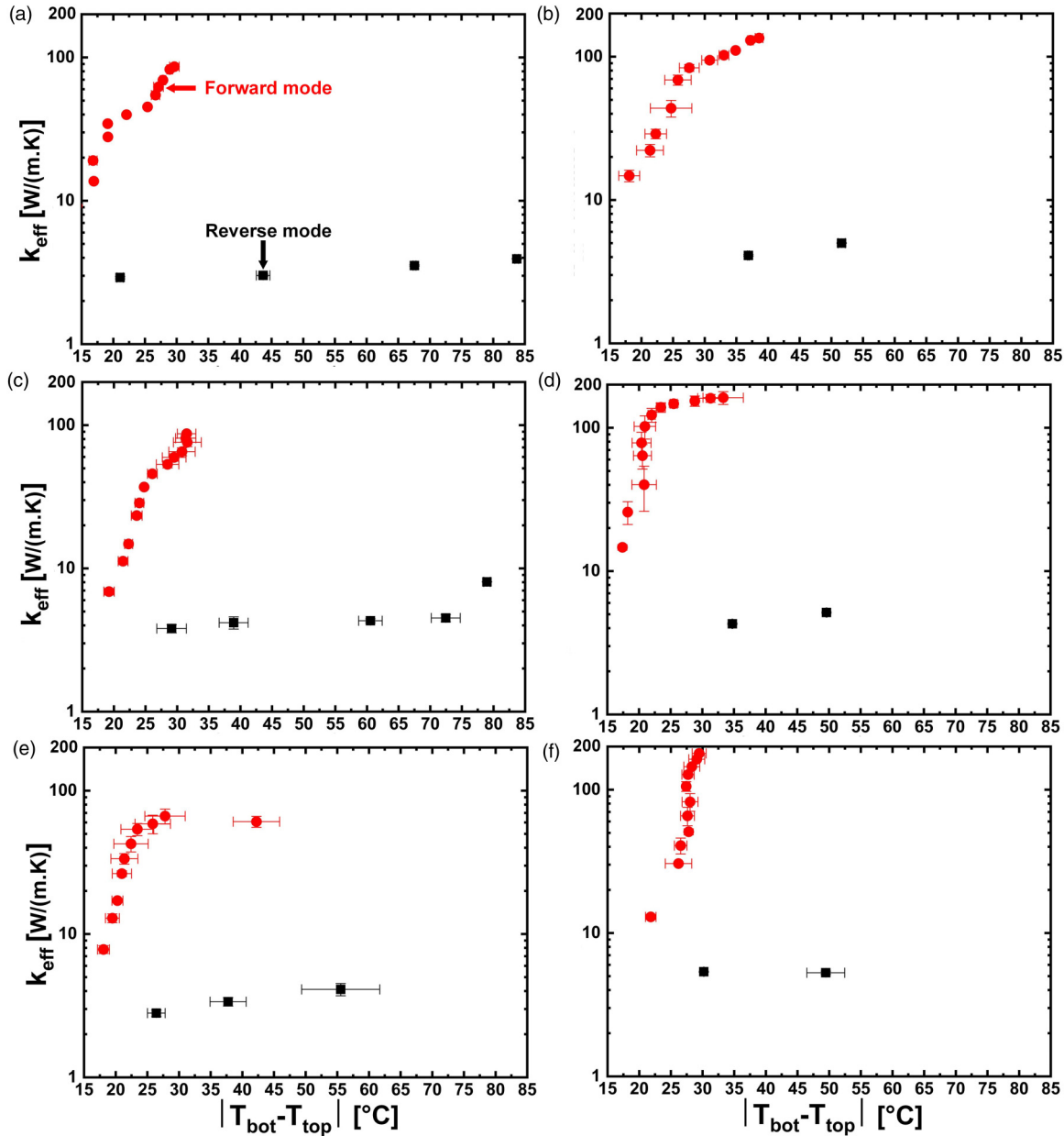


FIG. 9. Thermal-conductivity based TR characterization as a function of temperature difference for chambers having (a) coolant mass of 2 g and gap size of  $H = 1.27$  cm, (b) coolant mass of 2 g and  $H = 2.54$  cm, (c) coolant mass of 4 g and  $H = 1.27$  cm, (d) coolant mass of 4 g and  $H = 2.54$  cm, (e) coolant mass of 8 g and  $H = 1.27$  cm, and (f) coolant mass of 8 g and  $H = 2.54$  cm. Red circles and black squares represent forward and reverse mode, respectively.

2-g coolant mass can reach  $R_{th} = 3.9$  K/W in the temperature range of 35 to 45 °C while the  $H = 2.54$ -cm chamber reaches  $R_{th} = 5.7$  K/W. In other words, a 100% increase in the chamber height can result in a 46.2% increase in the thermal resistance. The thermal-resistance based TR effectiveness, calculated in Eq. (8), is also listed in Table I and used to evaluate the chamber performance. This thermal-resistance based definition eliminates the effect of chamber height. Generally, the thermal-resistance based TR effectiveness is close to the thermal-conductivity based TD for fill ratios less than 30%. Similarly, a taller chamber can obtain a relatively high thermal-resistance based TR effectiveness. However, for the case of fill ratio of 57.8%, in which the primary thermal

resistance comes from the macroscopic bulk water in the chamber, the thermal-resistance based TR effectiveness can reach 23.7 while the thermal-conductivity based TD is only 13.8. Therefore, using the thermal-resistance based TR effectiveness instead of the thermal-conductivity based TD may be more reasonable at large fill ratios in order to eliminate chamber height effects.

$$\zeta = (R_{th, re} - R_{th, for})/R_{th, for}, \tag{8}$$

where  $R_{th, re}$  is the thermal resistance of the reverse mode and  $R_{th, for}$  is the thermal resistance of the forward mode.

The application of the proposed TR to real systems has profound implications. For instance, thermal management

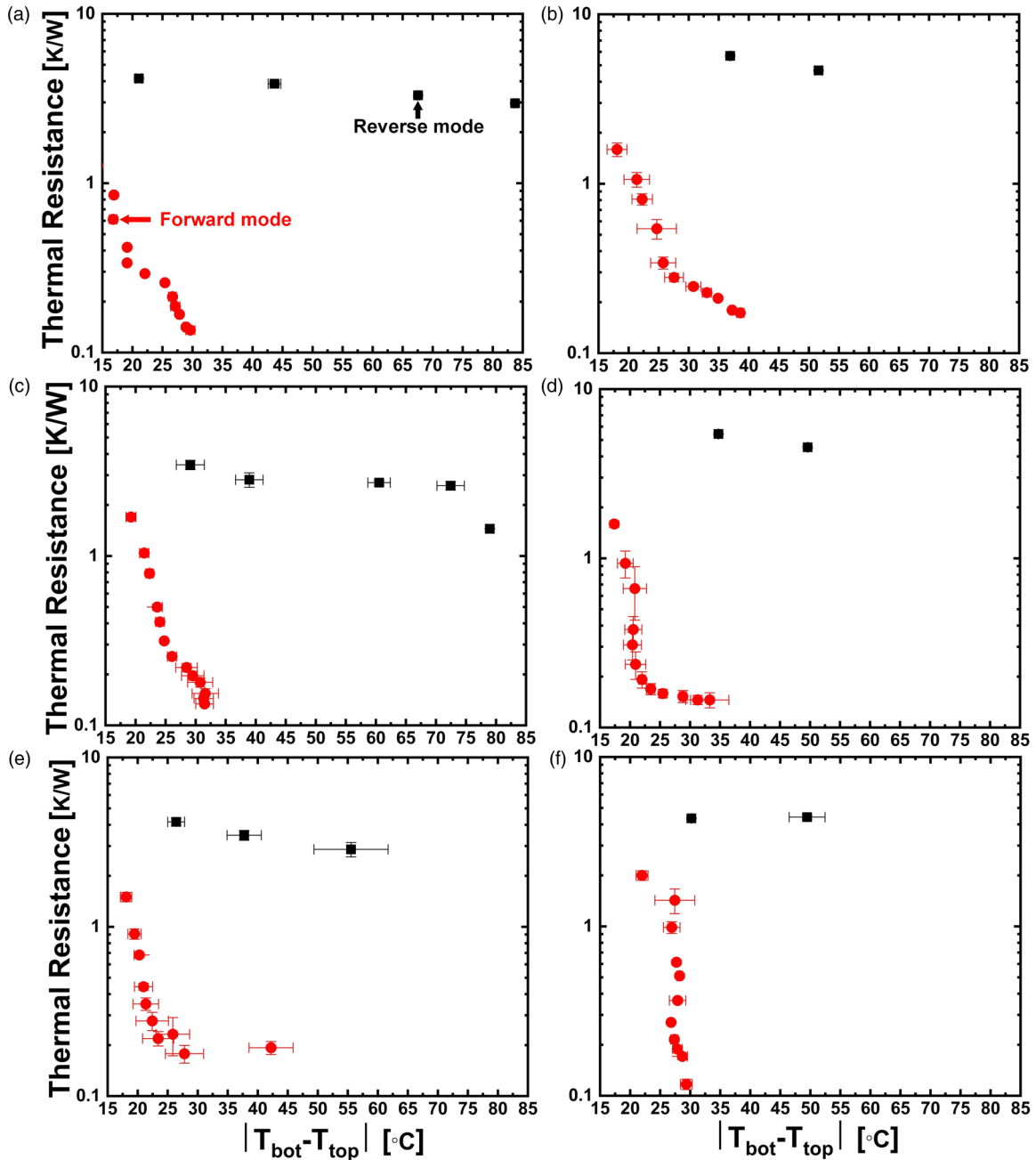


FIG. 10. Thermal-resistance based TR characterization and a function of temperature difference for chambers having (a) coolant mass of 2 g and gap size of  $H = 1.27$  cm, (b) coolant mass of 2 g and  $H = 2.54$  cm, (c) coolant mass of 4 g and  $H = 1.27$  cm, (d) coolant mass of 4 g and  $H = 2.54$  cm, (e) coolant mass of 8 g and  $H = 1.27$  cm, and (f) coolant mass of 8 g and  $H = 2.54$  cm. Red circles and black squares represent forward and reverse mode, respectively.

of temperature-sensitive electronics [42–47] such as GaN transistors in radar on hypersonic aircraft, where heat is only preferred to be able to flow from the internal volume of the vehicle (relatively low temperature) to the outer skin. During hypersonic flight, a relatively high temperature can be achieved on the outer skin due to aerodynamic heating, necessitating thermal rectification and blockage of heat flow to the internal components. Furthermore, the developed TR can be implemented in thermal management of space applications where the spacecraft skin is exposed to alternate high and low temperature conditions. When facing the sun, the spacecraft

skin can reach 150 °C when in earth orbit and up to 500 °C when in Mercury orbit, necessitating the need for efficient thermal rectification to prevent heat from flowing into the internal volume of the spacecraft, and enabling downsizing of heavy thermal management components. When facing free space (away from the sub), the skin reaches temperatures as low as 2 K, and the TR can facilitate efficient heat flow from internal to external regions to make the skin act as a heat sink.

In addition to rectification operating modes, the developed TR has added advantages of wickless transport of coolant to

the evaporating surface. Many aerospace applications involve high- $G$  conditions, particularly for in-atmosphere vehicle maneuvering, where the liquid inertia can prevent coolant from flowing to hot spots when regular wick-based or pumped solutions are used. The proposed nanostructured TR provides an opportunity to overcome inertial effects by using the kinetic energy of microscale droplet jumping where surface energy dominates body forces such as gravity.

Although promising, limitations exist to the devices developed here. First, the evaporator surface is a nanostructured interface devoid of any microscale wick capable of containing and pumping substantially thick liquid films. The lack of a microstructured wick results in bulk water contact with the superhydrophilic evaporator and most likely thick capillarity-dominated liquid layers on the superhydrophilic surface during reverse mode operation (evaporator on top, lack of a microscale wick to thin out the liquid). Although removal of a microscale wick results in better thermal performance from elimination of a key thermal resistance, the lack of a wick is disadvantageous due to reduced TD when operating the device in the reverse orientation (superhydrophilic evaporator on top, forward mode). Without the wick, the developed TR functions well with the orientation studied comprising the superhydrophilic evaporator on bottom and superhydrophobic condenser on top under the earth gravity (vector pointing from top to bottom). This gravitational dependence makes our devices act analogous to thermosyphon-based TRs. However, the TR devices developed here can only function well when placed in an orientation ensuring that the bottom is the evaporator and the top is the condenser, makes our design more of a thermosyphon-based TR. Furthermore, leaks present in the chamber also contribute to reduced TD.

Future work is needed to better understand the TR heat transfer performance under electric field application [48–50]. Furthermore, functional surface reliability and durability should be carefully considered [51–54]. Several studies have previously revealed clear and unavoidable degradation of nanostructured surfaces including the CuO structures used here [55,56]. Lastly, future work using a transparent spacer would enable the study of the fluid dynamics occurring inside the chamber such that water layer thickness can be quantified to precisely establish a predictive thermal resistance model.

#### IV. CONCLUSIONS

The performance of heat pipes or vapor chambers, along with thermal rectifiers (TRs) made from CuO-based nanostructured jumping-droplet vapor chambers, is analyzed. Two operational modes: forward and reverse modes, in addition to the combined effects of gap size, coolant mass, coolant fill ratio, and external electric field, are investigated. The main findings can be summarized as follows: (i) for heat transfer performance in the forward mode, the specific effective thermal conductivity of the adopted CuO nanostructured chamber can be 300% higher when compared to solid Cu, and is up to  $18.6\times$  that of the smooth Cu chamber. (ii) In the forward mode, smaller fill ratios result in higher effective thermal conductivity where a 50% decrease in the fill ratio can achieve a corresponding 60% increase in effective thermal conductivity. In contrast, the thermal resistance of the chamber is insensitive to the fill ratio. (iii) Externally applied electric fields have the potential to affect the thermal performance; however, due to experimental limitations, they were not capable of being quantified and need further investigation. (iv) Compared with the fill ratio, the gap size affects the effectiveness of the thermal rectification more significantly, with a doubling of gap size attaining a 182% increase in thermal-conductivity based thermal diodicity (TD). (v) Thermal-resistance based TR effectiveness instead of the thermal-conductivity based TD may be a better measure of real thermal rectification behavior when large fill ratios are used.

#### ACKNOWLEDGMENTS

This work was funded by the Center of Excellence for Integrated Thermal Management of Aerospace Vehicles and by the National Science Foundation Engineering Research Center for Power Optimization of Electro Thermal Systems (POETS) with Cooperative Agreement No. EEC-1449548. N.M. gratefully acknowledges funding support from the International Institute for Carbon Neutral Energy Research (Grant No. WPI-I2CNER), sponsored by the Japanese Ministry of Education, Culture, Sports, Science, and Technology. J.-X.W. would like to acknowledge the financial support from China Scholarship Council, which funded his visit to the University of Illinois where the work was conducted.

- 
- [1] B. Hu, D. He, L. Yang, and Y. Zhang, Thermal rectifying effect in macroscopic size, *Phys. Rev. E* **74**, 060201(R) (2006).
  - [2] W. Kobayashi, Y. Teraoka, and I. Terasaki, An oxide thermal rectifier, *Appl. Phys. Lett.* **95**, 171905 (2009).
  - [3] J.-X. Wang, W. Guo, K. Xiong, and S.-N. Wang, Review of aerospace-oriented spray cooling technology, *Prog. Aerosp. Sci.* **116**, 100635 (2020).
  - [4] C. Starr, The copper oxide rectifier, *Physics* **7**, 15 (1936).
  - [5] C. W. Chang, D. Okawa, A. Majumdar, and A. Zettl, Solid-state thermal rectifier, *Science* **314**, 1121 (2006).
  - [6] H. Wang, S. Hu, K. Takahashi, X. Zhang, H. Takamatsu, and J. Chen, Experimental study of thermal rectification in suspended monolayer graphene, *Nat. Commun.* **8**, 15843 (2017).
  - [7] B. Traipattanakul, C. Y. Tso, and C. Y. H. Chao, A phase-change thermal diode using electrostatic-induced coalescing-jumping droplets, *Int. J. Heat Mass Transfer* **135**, 294 (2019).
  - [8] N. Li and J. Ren, Non-reciprocal geometric wave diode by engineering asymmetric shapes of nonlinear materials, *Sci. Rep.* **4**, 6228 (2014).
  - [9] B. Li, J. Lan, and L. Wang, Interface Thermal Resistance between Dissimilar Anharmonic Lattices, *Phys. Rev. Lett.* **95**, 104302 (2005).
  - [10] Y. Yang, H. Chen, H. Wang, N. Li, and L. Zhang, Optimized thermal rectification of heterojunctions under Fourier law, *Phys. Rev. E* **98**, 042131 (2018).
  - [11] C. Y. Tso and C. Y. Chao, Solid-state thermal diode with shape memory alloys, *Int. J. Heat Mass Transfer* **93**, 605 (2016).

- [12] M. J. Martínez-Pérez, A. Fornieri, and F. Giazotto, Rectification of electronic heat current by a hybrid thermal diode, *Nat. Nanotechnol.* **10**, 303 (2015).
- [13] C. R. Otey, W. T. Lau, and S. Fan, Thermal Rectification through Vacuum, *Phys. Rev. Lett.* **104**, 154301 (2010).
- [14] S. Basu and M. Francoeur, Near-field radiative transfer based thermal rectification using doped silicon, *Appl. Phys. Lett.* **98**, 113106 (2011).
- [15] W. Kobayashi, D. Sawaki, T. Omura, T. Katsufuji, Y. Moritomo, and I. Terasaki, Thermal rectification in the vicinity of a structural phase transition, *Appl. Phys. Exp.* **5**, 027302 (2012).
- [16] R. Chen, Y. Cui, H. Tian, R. Yao, Z. Liu, Y. Shu, C. Li, Y. Yang, T. Ren, G. Zhang, and R. Zou, Controllable thermal rectification realized in binary phase change composites, *Sci. Rep.* **5**, 8884 (2015).
- [17] X. Fang and L. Xia, Heating performance investigation of a bidirectional partition fluid thermal diode, *Renew. Energy* **35**, 679 (2010).
- [18] M. Edalatpour, K. R. Murphy, R. Mukherjee, and J. B. Boreyko, Bridging-droplet thermal diodes, *Adv. Funct. Mater.* **30**, 2004451 (2020).
- [19] F. Wiedenheft, H. A. Guo, X. Qu, J. B. Boreyko, F. Liu, K. Zhang, F. Eid, A. Choudhury, Z. Li, and C. H. Chen, Hotspot cooling with jumping-drop vapor chambers, *Appl. Phys. Lett.* **110**, 141601 (2017).
- [20] J. B. Boreyko, Y. Zhao, and C. Chen, Planar jumping-drop thermal diodes, *Appl. Phys. Lett.* **99**, 234105 (2011).
- [21] J. B. Boreyko and C. Chen, Vapor chambers with jumping-drop liquid return from superhydrophobic condensers, *Int. J. Heat Mass Transfer* **61**, 409 (2013).
- [22] N. Miljkovic, D. J. Preston, R. Enright, and E. N. Wang, Electrostatic charging of jumping droplet, *Nat. Commun.* **4**, 2517 (2013).
- [23] D. Attinger, C. Frankiewicz, A. R. Betz, T. M. Schutzius, R. Ganguly, A. Das, C.-J. Kim, and C. M. Megaridis, Surface engineering for phase change heat transfer: A review, *MRS Energy & Sustainability* **1**, 4 (2014).
- [24] N. Miljkovic, D. J. Preston, R. Enright, and E. N. Wang, Jumping-droplet electrostatic energy harvesting, *Appl. Phys. Lett.* **105**, 013111 (2014).
- [25] J. Oh, P. Birbarah, T. Foulkes, S. L. Yin, M. Rentauskas, J. Neely, R. C. N. Pilawa-Podgurski, and N. Miljkovic, Jumping-droplet electronics hot-spot cooling, *Appl. Phys. Lett.* **110**, 123107 (2017).
- [26] D. Ding, L. Chen, D. Sun, L. Zhao, and N. Wang, New device for calibration of leakage rate of spacecraft cabin balance valve, *Vacuum*, **183**, 109796 (2021).
- [27] S. Sett, P. Sokalski, K. Boyina, L. Li, K. F. Rabbi, H. Auby *et al.*, Stable dropwise condensation of ethanol and hexane on rationally-designed ultra-scalable nanostructured lubricant-infused surfaces, *Nano Lett.* **19**, 5287 (2019).
- [28] S. Sett, P. Sokalski, M. Mehta, K. F. Rabbi, A. Gunay, and N. Miljkovic, Transient pulse condensation, *Appl. Phys. Lett.* **117**, 091602 (2020).
- [29] J.-X. Wang, Y.-Z. Li, J.-X. Li, C. Li, Y. Zhang, and X.-W. Ning, A gas-atomized spray cooling system integrated with an ejector loop: Ejector modeling and thermal performance analysis, *Energy Convers. Manage.* **180**, 106 (2019).
- [30] J. Cho, D. J. Preston, Y. Zhu, and E. N. Wang, Nanoengineered materials for liquid–vapour phase-change heat transfer, *Nat. Rev. Mater.* **2**, 16092 (2016).
- [31] K. H. Chu, Y. S. Young, R. Enright, C. R. Buie, and E. N. Wang, Hierarchically structured surfaces for boiling critical heat flux enhancement, *Appl. Phys. Lett.* **102**, 151602 (2013).
- [32] J. L. Plawsky, A. G. Fedorov, S. V. Garimella, H. B. Ma, S. C. Maroo, L. Chen, and Y. Nam, Nano- and microstructures for thin-film evaporation—A review, *Nanoscale Microsc. Therm.* **18**, 251 (2014).
- [33] N. Miljkovic, R. Enright, and E. N. Wang, Modeling and optimization of superhydrophobic condensation, *J. Heat Transfer – Trans. ASME*, **135**, 111004 (2013).
- [34] X. Yan, Y. Qin, F. Chen, G. Zhao, S. Sett, M. J. Hoque, K. F. Rabbi, X. Zhang *et al.*, Laplace pressure driven single-droplet jumping on structured surfaces, *ACS Nano*, **14**, 12796 (2020).
- [35] J. Ma, S. Sett, H. Cha, X. Yan, and N. Miljkovic, Recent developments, challenges, and pathways to stable dropwise condensation: A perspective, *Appl. Phys. Lett.* **116**, 260501 (2020).
- [36] T. Foulkes, J. Oh, P. Sokalski, L. Li, S. Sett, J. Sotelo, X. Yan *et al.*, Jumping droplets electronics cooling: Promise versus reality, *Appl. Phys. Lett.* **116**, 203701 (2020).
- [37] H. Cha, H. Vahabi, A. Wu, S. Chavan, M. K. Kim, S. Sett, S. A. Bosch, and W. Wang, Dropwise condensation on solid hydrophilic surfaces, *Sci. Adv.* **6**, eaax0746 (2020).
- [38] T. Foulkes, S. Sett, P. Sokalski, J. Oh, and N. Miljkovic, Fundamental limits of jumping droplet heat transfer, *Appl. Phys. Lett.* **116**, 093701 (2020).
- [39] P. Birbarah, S. Chavan, and N. Miljkovic, Numerical simulation of jumping droplet condensation, *Langmuir* **35**, 10309 (2019).
- [40] J. Wang, Y. Li, X. Liu, C. Shen, H. Zhang, and K. Xiong, Recent active thermal management technologies for the development of energy-optimized aerospace vehicles in China, *Chin. J. Aeronaut.*
- [41] J.-X. Wang, Y.-Z. Li, J.-X. Li, C. Li, K. Xiong, and X.-W. Ning, Enhanced heat transfer by an original immersed spray cooling system integrated with an ejector, *Energy* **158**, 512 (2018).
- [42] J. X. Wang, Y. Z. Li, X. K. Yu, G. C. Li, and X. Y. Ji, Investigation of heat transfer mechanism of low environmental pressure large-space spray cooling for near-space flight systems, *Int. J. Heat Mass Transfer* **119**, 496 (2020).
- [43] B. Kwon, T. Foulkes, T. Yang, N. Miljkovic, and W. P. King, Air jet impingement cooling of electronic devices using additively manufactured nozzles, *IEEE Trans. Compon. Packag., Manuf. Technol.* **10**, 220 (2020).
- [44] C. Barth, T. Foulkes, O. Azofeifa, J. Colmenares, K. Coulson, N. Miljkovic, and R. C. N. Pilawa-Podgurski, Design, operation and loss characterization of a 1 kW GaN-based 3-level converter at cryogenic temperatures, *IEEE Trans. Power Electr.* **35**, 12040 (2020).
- [45] P. Birbarah, T. Gebrael, T. Foulkes, A. Stillwell, A. Moore, N. Miljkovic, and R. C. N. Pilawa-Podgurski, Water immersion cooling of high power density electronics, *Int. J. Heat Mass Transfer* **147**, 118918 (2020).
- [46] J. X. Wang, Y. Z. Li, M. L. Zhong, and H. S. Zhang, Investigation on a gas-atomized spray cooling upon flat and micro-structured surfaces, *Int. J. Therm. Sci.* **161**, 106751 (2021).

- [47] J. X. Wang, Y. Z. Li, G. C. Li, K. Xiong, and X. Ning, Investigation of a gravity-immune chip-level spray cooling for thermal protection of laser-based wireless power transmission system, *Int. J. Heat Mass Transfer* **114**, 715 (2017).
- [48] A. Shahriari, P. Birbarah, J. Oh, N. Miljkovic, and V. Bahadur, Electric field-based control and enhancement of boiling and condensation, *Nanosc. Microsc. Therm.* **21**, 102 (2017).
- [49] P. Birbarah, Z. Li, A. Pauls, and N. Miljkovic, A comprehensive model of electric-field-enhanced jumping-droplet condensation on superhydrophobic surfaces, *Langmuir* **31**, 7885 (2015).
- [50] N. Miljkovic, D. J. Preston, R. Enright, and E. N. Wang, Electric-field-enhanced condensation on superhydrophobic nanostructured surfaces, *ACS Nano* **7**, 11043 (2013).
- [51] H. C. Chang, M. C. Rajagopal, M. J. Hoque, J. Oh, L. Li, J. Li, H. Zhao *et al.*, Composite structured surfaces for durable dropwise condensation, *Int. J. Heat Mass Transfer* **156**, 119890 (2020).
- [52] M. Bakir, C. N. Henderson, J. L. Meyer, J. Oh, N. Miljkovic, M. Kumosa, J. Economy, and I. Jasiuk, Effects of environmental aging on physical properties of aromatic thermosetting copolyester matrix neat and nanocomposite foams, *Polym. Degrad. Stabil.* **147**, 49 (2018).
- [53] J. Ma, D. G. Cahill, and N. Miljkovic, Condensation induced blistering as a measurement technique for the adhesion energy of nanoscale polymer films, *Nano Lett.* **20**, 3918 (2020).
- [54] J. Ma, H. Cha, M. K. Kim, D. G. Cahill, and N. Miljkovic, Condensation induced delamination of nanoscale hydrophobic films, *Adv. Funct. Mater.* **29**, 1905222 (2019).
- [55] F. Zhou, Y. Liu, S. N. Joshi, E. M. Dede, X. Chen, and J. A. Weibel, Vapor chamber with thermal diode and switch functions, *16th IEEE Intersociety Conference on Thermal and Thermomechanical Phenomena in Electronic Systems (ITherm)* (IEEE, Orlando, FL, 2017), pp. 521.
- [56] X. Yan, Z. Huang, S. Sett, J. Oh, H. Cha, L. Li, L. Feng, Y. Wu, C. Zhao, D. Orejon, F. Chen, and N. Miljkovic, Atmosphere-mediated superhydrophobicity of rationally designed micro/nanostructured surfaces, *ACS Nano*, **13**, 4160 (2019).